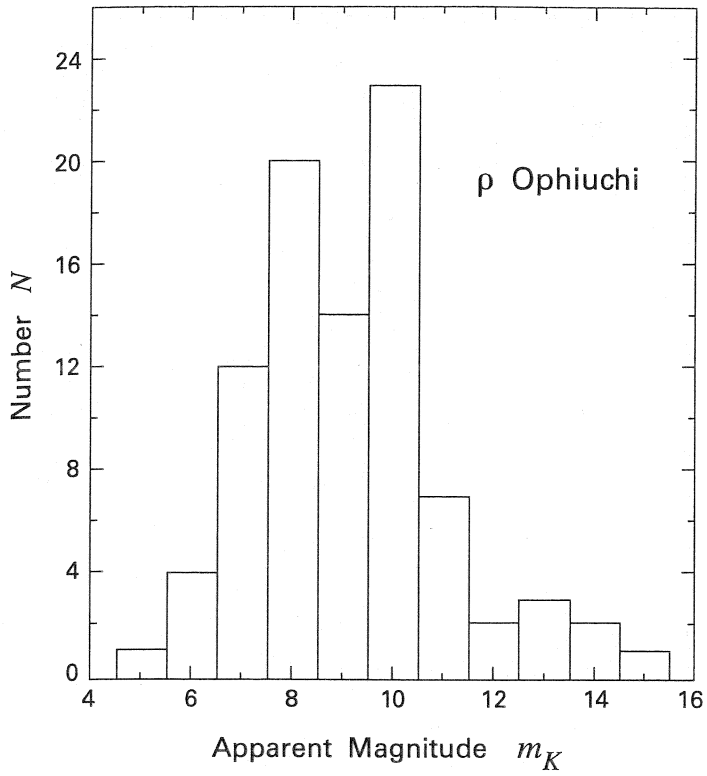

Figure 4.5 Luminosity function in the K band for 90 stars in the L1688 region of ρ Ophiuchi.

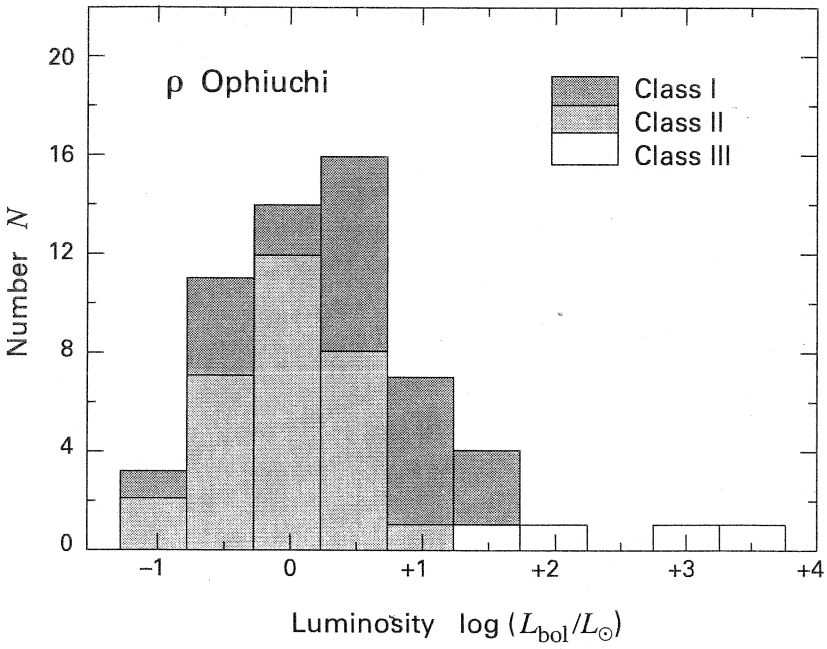

Figure 4.6 Bolometric luminosity function for 55 ρ Ophiuchi stars, again in L1688. The distribution among three spectral classes is indicated.

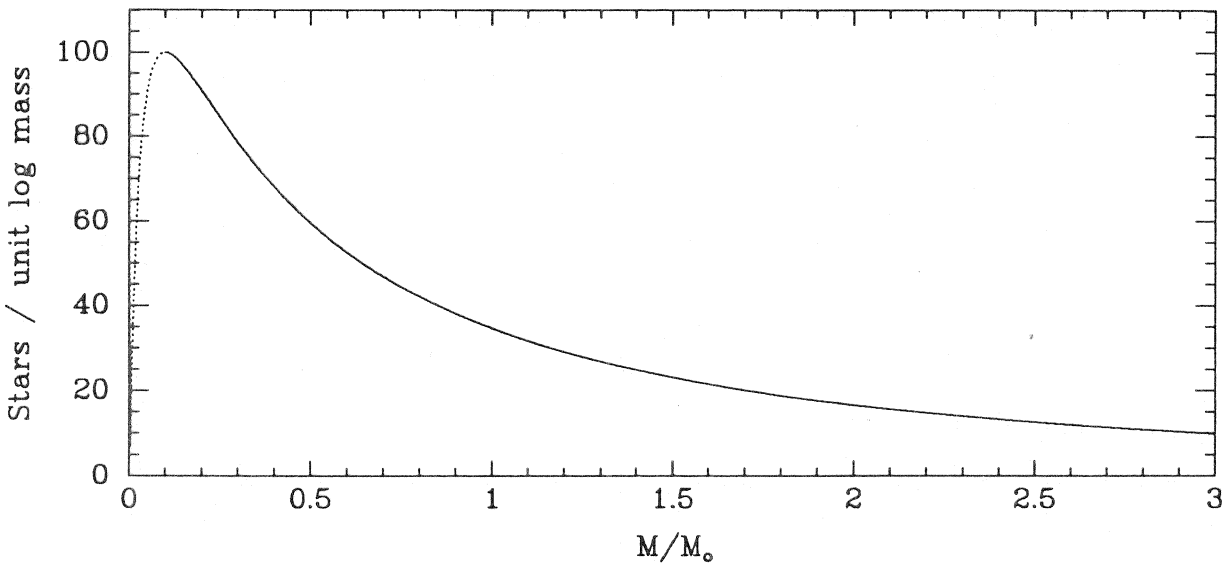

Figure 18. Log-normal model IMF for low-mass stars according to Zinnecker (1984*b*). The IMF shown here is the relative number of newly born stars as a function of mass (in units of solar mass) per unit log mass interval. This curve is very similar to the well-known Miller-Scalo IMF, except for the (log-normally continued) extrapolation to substellar masses.

are not massive enough to ignite hydrogen burning (D'Antona and Mazzitelli

stars of a given M_V first appear. This function is normalized to unity: $\int \Psi(M_V)\, dM_V = 1$. Resetting M_V^* to that magnitude for which $t_{\rm MS} = t_{\rm gal}$ precisely, we can write the general luminosity function as an integral over time, where the integration limits depend on M_V:

$$\Phi(M_V) = \begin{cases} \int_{t_{\rm gal}-t_{\rm MS}}^{t_{\rm gal}} dt\, \dot{m}_*(t)\, \Psi(M_V)\, [2\, H(M_V)]^{-1} & \text{if } M_V < M_V^* \\ \int_0^{t_{\rm gal}} dt\, \dot{m}_*(t)\, \Psi(M_V)\, [2\, H(M_V)]^{-1} & \text{if } M_V \geq M_V^* \ . \end{cases} \tag{4.4}$$

In writing equation (4.4), we have ignored any possible time-dependence in $\Psi(M_V)$ or $H(M_V)$. Furthermore, we are actually interested in the appearance of *main-sequence* stars with various magnitudes, while $\Phi(M_V)$ encompasses bright field stars that are giants and supergiants. Accordingly, the luminosity function on the left side of equation (4.4) must be diminished at the lowest values of M_V, corresponding to the brightest stars.

After making this correction, knowledge of the main-sequence lifetimes $t_{\rm MS}(M_V)$ allows us to invert equation (4.4) and obtain $\Psi(M_V)$, *provided* we know the rate $\dot{m}_*(t)$. Neither theory nor observation is of much help in this regard, beyond the general statement that $\dot{m}_*(t)$ should diminish with time. Fortunately, the final result is rather insensitive to the prescription adopted here, so we follow the standard expedient of ignoring the time dependence and adopting a fixed rate. With $\Psi(M_V)$ in hand, it is a straightforward matter to apply bolometric corrections and obtain the relative birthrates of stars as a function of $L_{\rm bol}$ rather than M_V. This is $\Psi(L_{\rm bol})$, the form of the initial luminosity function already shown in Figure 4.13. As anticipated, the curve here is smoother than $\Phi(M_V)$, since it lacks the age-dependent falloff for the brightest stars.

4.5.2 Character of the Mass Distribution

Our true goal, however, is the distribution at birth of various stellar *masses*. We accordingly define $\xi\,(M_*)$ to be the *initial mass function (IMF)*, the relative number of stars produced per unit mass interval. Again normalizing this function to unity, we have simply

$$\xi\,(M_*) = \Psi(M_V) \frac{dM_V}{dM_*} \ . \tag{4.5}$$

The derivative on the righthand side refers to variations along the main sequence and can be obtained numerically from Table 1.1 or its equivalent.[3]

Historically, E. E. Salpeter proceeded in the manner we have outlined to find that $\xi\,(M_*)$ varies as M_*^γ, with $\gamma = -2.35$. This simple power law is still frequently employed to obtain approximate results, but has long since been supplanted by other investigations using more extensive data. Figure 4.22 displays the results of a later study. For convenience, we may approximate the mass function as a sequence of power laws:

$$\xi\,(M_*) = \begin{cases} C\ (M_*/M_\odot)^{-1.2} & 0.1 < M_*/M_\odot < 1.0 \\ C\ (M_*/M_\odot)^{-2.7} & 1.0 < M_*/M_\odot < 10 \\ 0.40\, C\ (M_*/M_\odot)^{-2.3} & 10 < M_*/M_\odot \ , \end{cases} \tag{4.6}$$

[3] Many authors define the IMF as the relative number of stars per *logarithmic* mass interval, *i. e.*, as $M_*\, \xi(M_*)$. The reader should check carefully in each case.

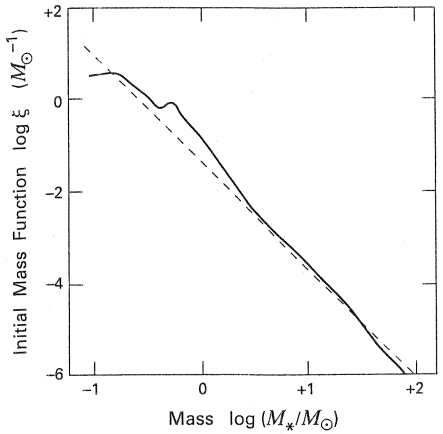

Figure 4.22 Initial mass function for solar neighborhood stars. The dashed line has the same slope as Salpeter's power law.

where C is a normalization constant. It is apparent that $\xi\,(M_*)$ is considerably flatter than Salpeter's function (*dashed line*) below $1.0\, M_\odot$ and approaches it for $M_* \gtrsim 10\, M_\odot$. Both of these general features have been amply confirmed. Our simple power law does not capture the broad maximum near $0.1\, M_\odot$ seen in the figure, but the true behavior at the lowest masses remains unclear. Their small luminosities make objects in this regime difficult to detect. After extensive searches, a growing population of *brown dwarfs*, *i. e.*, objects less massive than the hydrogen-burning limit of $0.08\, M_\odot$, is presently being uncovered. These and other data indicate that $\xi\,(M_*)$ is relatively flat near the brown-dwarf limit. Establishing its precise form will require additional effort.

This lingering uncertainty should not obscure the essential message of Figure 4.22. Within any volume undergoing star formation, the number of new stars per unit mass falls rapidly above roughly $0.1\, M_\odot$. If we make the simplifying assumption that $\xi\,(M_*)$ is constant below this value, then equation (4.6) implies that half of all stars are produced with $M_* \geq 0.2\, M_\odot$. Only 12 percent have masses exceeding $1\, M_\odot$, while the fraction drops to 0.3 percent for stars above $10\, M_\odot$. Conversely, 70 percent of stars have $M_* \geq 0.1\, M_\odot$. We conclude that *the star formation process yields objects with a characteristic mass of a few tenths of* $M_\odot$. Things might have been otherwise. One could imagine stars forming with a pure power-law mass spectrum down to some very low level at the planetary scale. That this is *not* the case is surely significant. Unfortunately, current theory cannot explain, in any convincing manner, the form of $\xi\,(M_*)$. Even the origin of the basic mass scale itself remains uncertain. Needless to say, we shall revisit this central issue in later chapters.

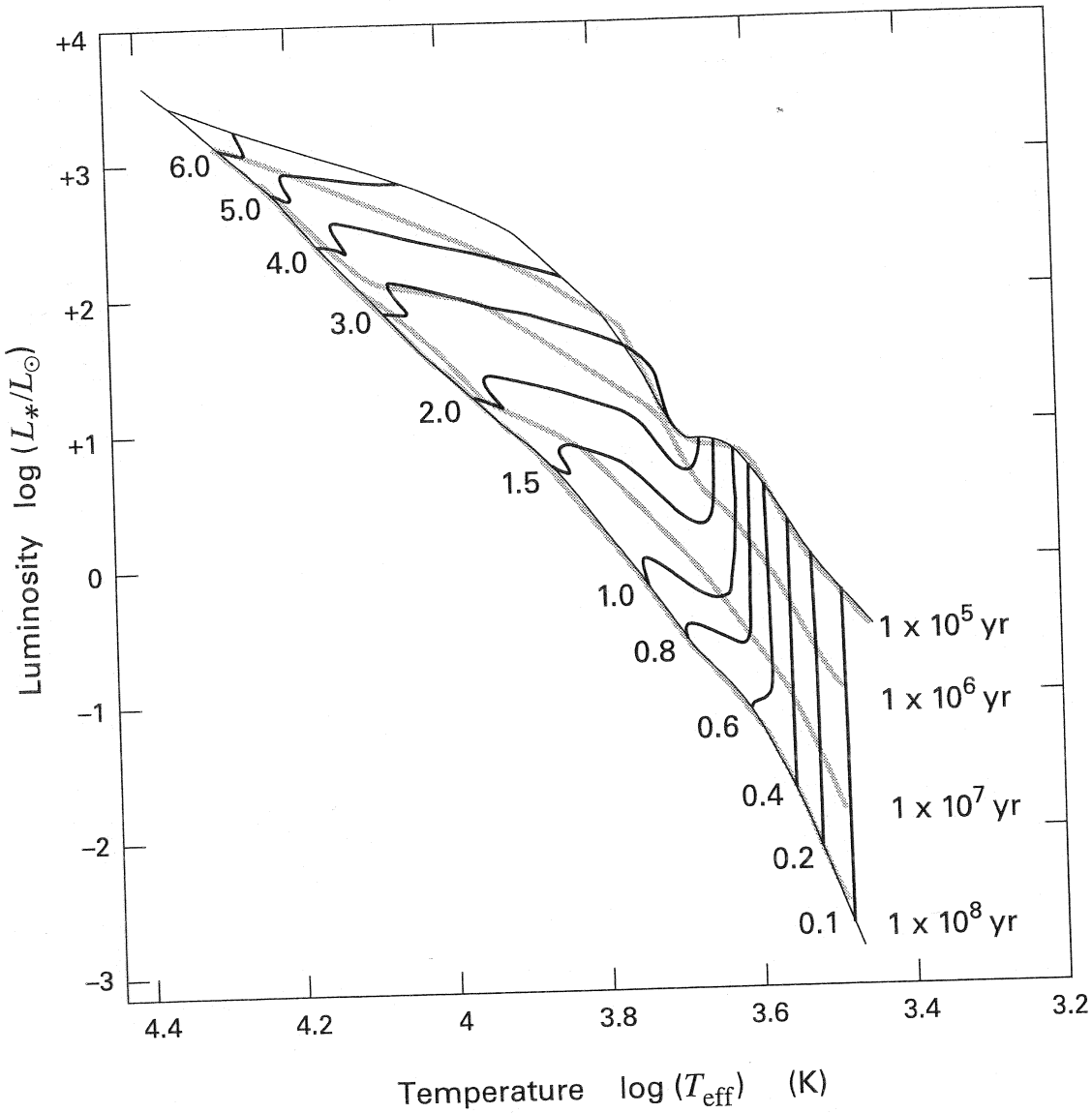

Figure 1.18 Pre-main-sequence evolutionary tracks. Each track is labeled by the stellar mass in units of $M_\odot$. The grey curves are isochrones, labeled in yr. The $t = 0$ isochrone coincides with the birthline, the lighter solid curve at the top. Note that the $t = 1 \times 10^8$ yr isochrone nearly matches the ZAMS, the lighter solid curve at the bottom.

The pre-main-sequence phase of evolution is not the first. At an earlier epoch, stars are still forming out of the gravitational collapse of their parent dense cores. Such *protostars* are even more luminous than pre-main-sequence stars, but are so obscured by interstellar dust that their emitted radiation lies entirely in the infrared and longer wavelengths. Under these circumstances, $T_{\rm eff}$ cannot be found by the traditional methods. Indeed, the character of the observed spectrum reflects more the properties of the dust surrounding the star than the stellar surface. Protostars therefore cannot be placed in a conventional HR diagram, and their identification within molecular clouds is still not secure.

Returning to pre-main-sequence evolution, we noted earlier that the contraction of any star causes its central temperature to rise. As long as the stellar mass exceeds 0.08 $M_\odot$, the temperature eventually reaches a value (near 10^7 K) where hydrogen fusion begins. Just at this point, the star is said to be on the *zero-age main sequence (ZAMS)*, and the corresponding relation between L_* (or $L_{\rm bol}$) and $T_{\rm eff}$ marks a rather precise locus in the HR diagram. The ZAMS is the curve actually shown in both Figures 1.15 and 1.18, and its properties are also listed in Ta-

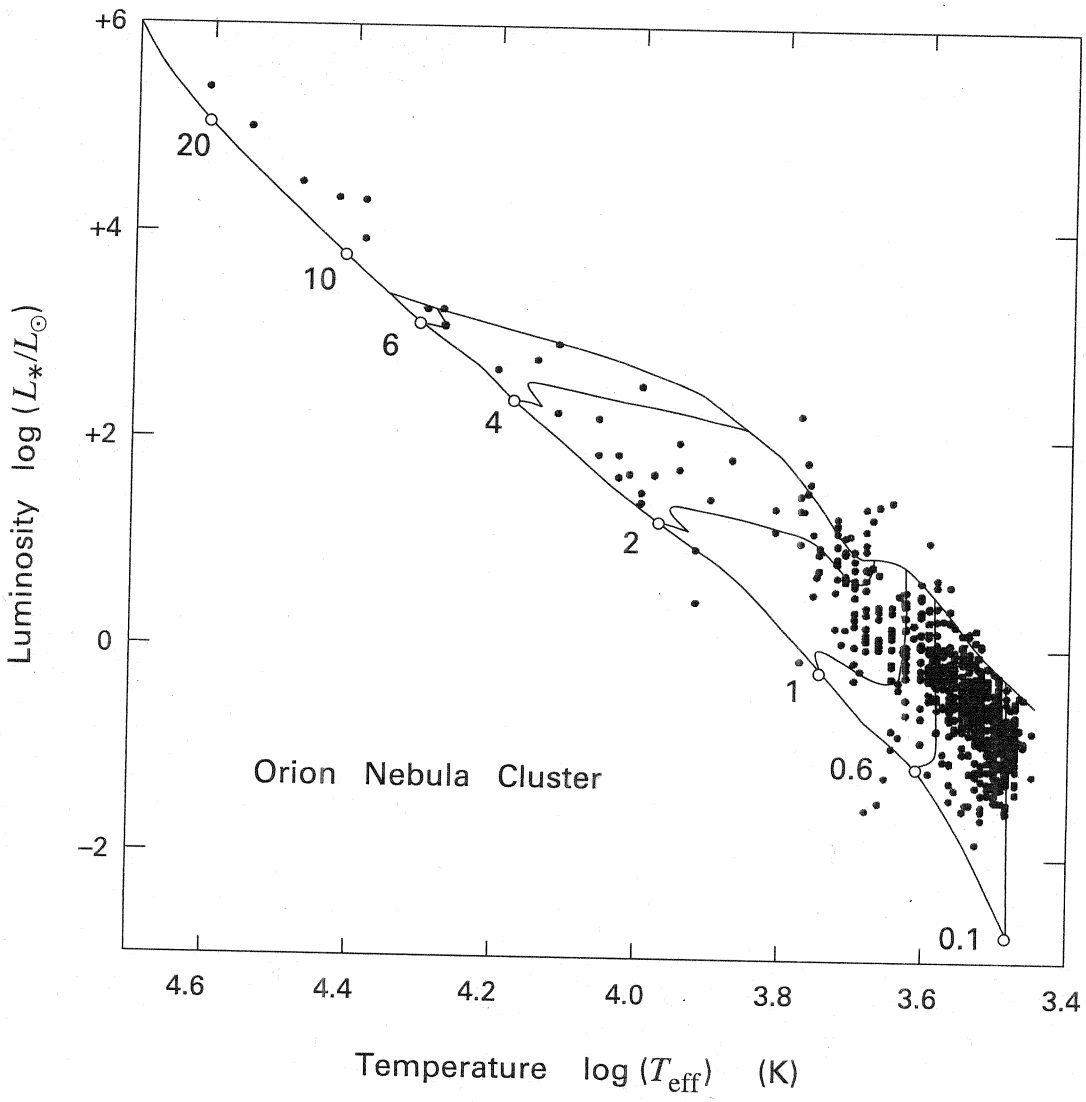

Figure 12.29 HR diagram of the Orion Nebula Cluster. The birthline, ZAMS, and selected pre-main-sequence tracks are also shown. Stellar masses for the tracks are given in solar units.

the birthrate function $C(t)$ employed in the statistical model should more properly increase with time.

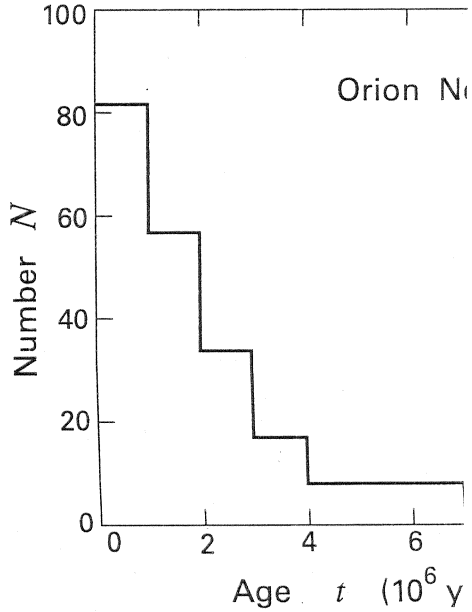

The rise of star formation prior t
undergone bulk contraction, presuma
contraction proceeds to higher densit
or open clusters. At any time, moreo
In our example of Orion, more detail
for stars with $M_* \gtrsim 5\,M_\odot$. Numerica
higher-mass objects *cannot* be the res
a few million years. These calculati
gas at all. Nevertheless, their essentia
drift to their present locations, but m

12.5.4 Birth of OB Associat

Creation of the O stars themselves

Table 16.1 The Theoretical Birthline

Mass ($M_\odot$)	Radius ($R_\odot$)	$\log L_*$ ($L_\odot$)	$\log T_{\rm eff}$ (K)	Δt_D (yr)	$t_{\rm ZAMS}$ (yr)
0.1	2.49	−0.28	3.49	1.5×10^6	3.7×10^8
0.2	2.52	−0.01	3.52	8.5×10^5	2.4×10^8
0.4	2.70	+0.27	3.56	3.0×10^5	1.1×10^8
0.8	4.32	+0.78	3.61	2.7×10^4	5.2×10^7
1.0	4.92	+0.85	3.63	6.9×10^3	3.2×10^7
1.5	5.09	+0.89	3.65	0	1.2×10^7
2.0	4.94	+0.90	3.67	0	8.4×10^6
3.0	5.66	+0.94	3.70	0	2.0×10^6
4.0	10.2	+2.09	3.84	1.4×10^4	8.2×10^5
5.0	8.20	+2.83	4.05	8.3×10^3	2.3×10^5
6.0	4.62	+3.24	4.27	1.1×10^3	2.9×10^4
7.0	3.28	+3.40	4.32	7.0×10^1	8.5×10^3
8.0	3.11	+3.55	4.36	0	0

The predicted birthline location clearly depends on the results of *both* protostar and pre-main-sequence theory. Deferring consideration of the latter, how sensitive is this location to the infall model? Given the considerable uncertainty regarding the infall phase, one must hope that the precise value of $\dot{M}$, its temporal behavior, or even the geometric pattern of infall, do not strongly influence the curve's location. Fortunately, this appears to be the case.

Consider the value of $\dot{M}$, assumed for the moment to be temporally constant. We saw in Chapter 10 how rates of 10^{-6} to 10^{-5} $M_\odot$ yr^{-1} are expected from the dynamics of inside-out collapse, in conjunction with the measured temperatures of dense cores. (The central relation connecting $\dot{M}$ and this temperature is equation (10.31).) But how does the birthline itself respond to a shift in the infall rate? The left panel of Figure 11.8 shows that the protostellar radius, at a given mass, diminishes for lower $\dot{M}$. Slower buildup of its mass gives the protostar more time to radiate internal energy and therefore shrink. Nevertheless, over the indicated range in $\dot{M}$, the radius change is severely restricted at subsolar masses. The reason, we recall, is the thermostatic effect of deuterium fusion. Although present in small quantities, this fuel effectively constrains the radius by altering the nuclear energy output during the main accretion phase. In calculations where deuterium fusion is artificially suppressed, the mass-radius curve undergoes a larger shift when $\dot{M}$ is altered. (See the right panel of Figure 11.8.)

Figure 16.3 shows the effect on the birthline of altering the infall rate, for the same $\dot{M}$-range as in Figure 11.8. As expected, inclusion of deuterium assures a relatively narrow spread in the predicted birthline. In contrast, the maximum luminosities for pre-main-sequence stars would have a larger dispersion in the hypothetical situation of zero deuterium abundance. To summarize, we now have one clue why the observed stellar groups show a rather sharp boundary in the HR diagram. This reasoning implies, incidentally, that any rise in the estimated deuterium abundance relative to hydrogen in the interstellar medium, a matter of ongoing investigation and here taken to be $[{\rm D/H}] = 2.5 \times 10^{-5}$, would tighten the theoretical boundary even more.

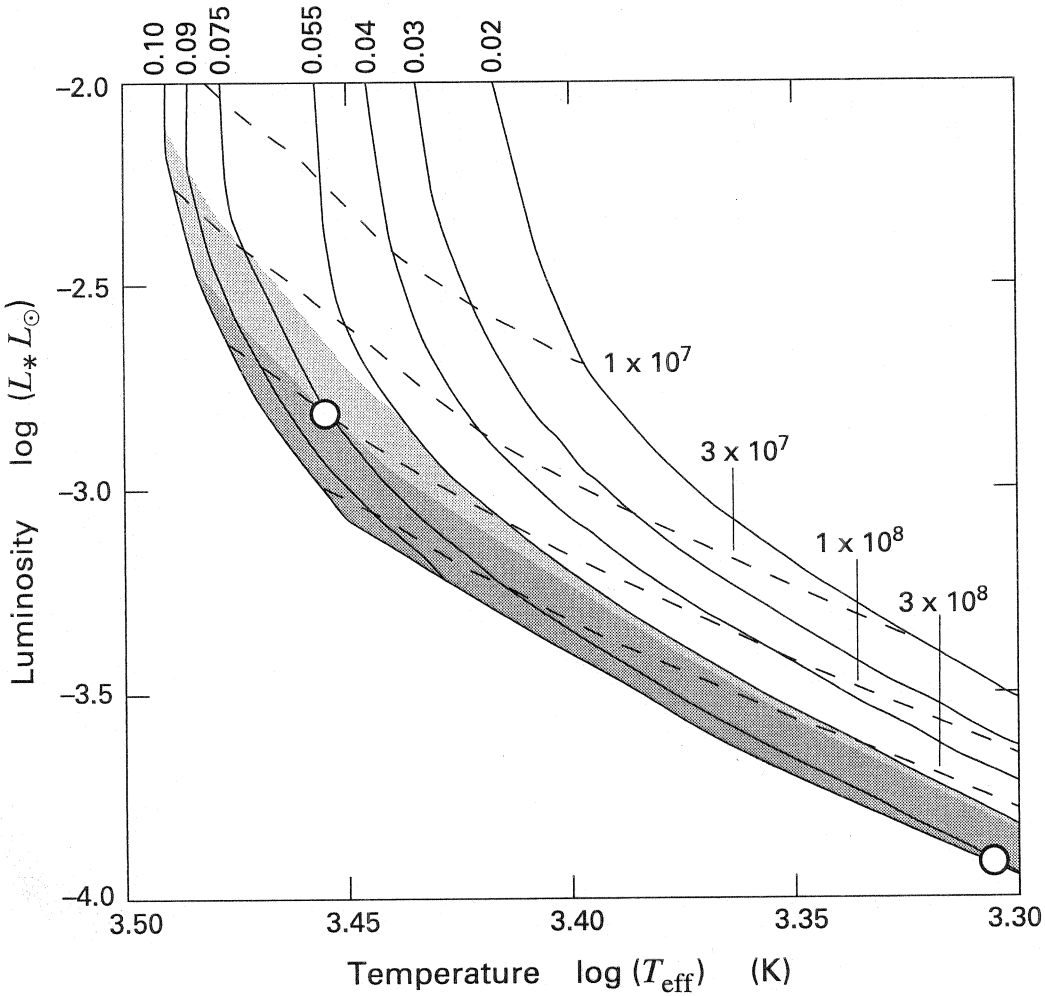

Figure 16.13 Evolutionary tracks of very low-mass stars and brown dwarfs. The corresponding masses, in solar units, and isochrones are also indicated. The light and dark shading signify the predicted depletion of surface lithium, as in Figure 16.10. Also shown is the point where a 0.075 $M_\odot$ star depletes 90 percent of its lithium (*upper open circle*), and where the object ignites hydrogen (*lower open circle*).

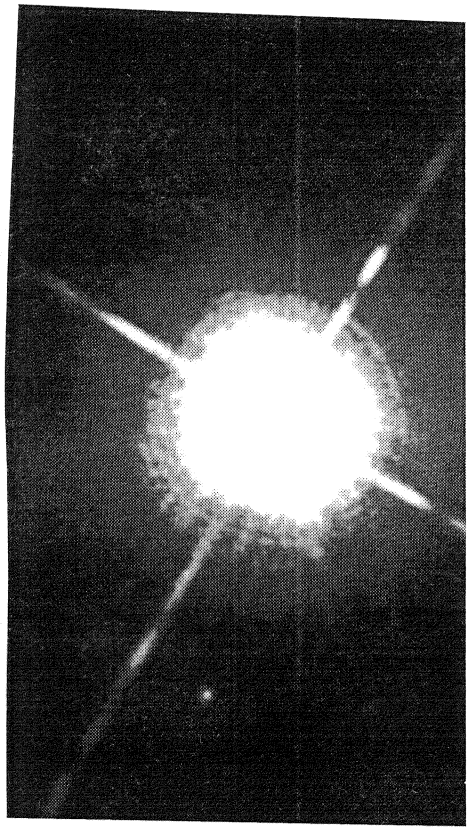

Figure 16.13 also displays the regi
scheme as Figure 16.10. The upper bo
This curve is parametrized by either th
the intersection of the boundary with
and below never achieve a central te
the upper boundary of the lightly sha
0.055 $M_\odot$ track but does not cross it.
but are eventually unable to ignite ev
times the mass of Jupiter, properly sig

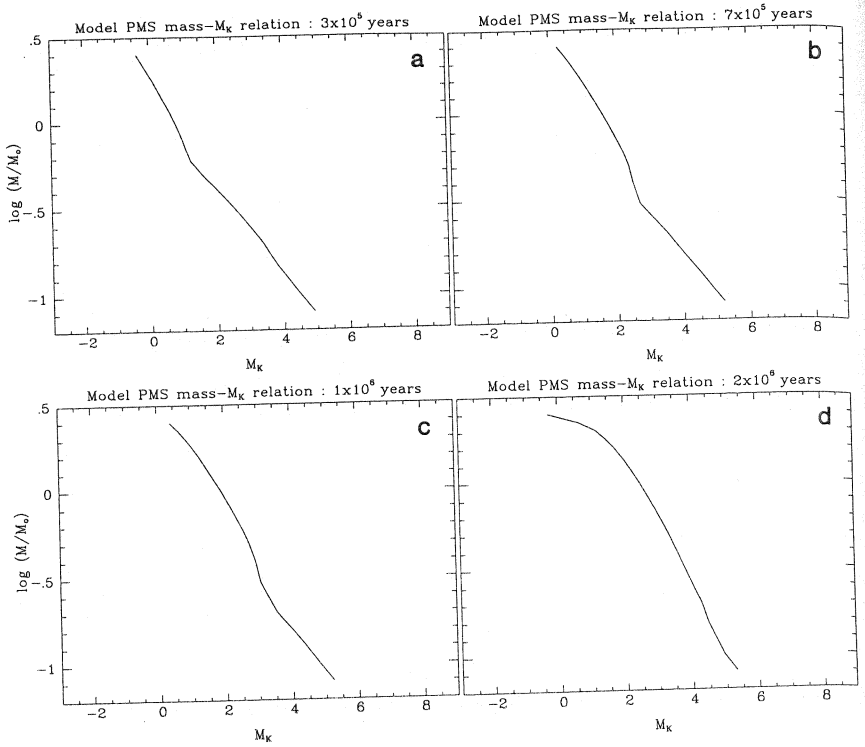

Figure 1 a,b,c,d. Time-dependent mass–M_K luminosity relations, as derived from homogeneous tracks of pre-main-sequence evolution calculated and kindly provided by I. Mazzitelli. Four ages are shown: 0.3, 0.7, 1, and 2 Myr.

mass–M_K relation and corresponding spectral types for main-sequence stars. Also note that 0.3 $M_\odot$ corresponds to $\log M = -0.5$ in these diagrams.

At 0.1 Myr (not shown), the shape of the KLF largely reflects the shape of the Miller-Scalo IMF, i.e., turning down and flattening towards the lower masses, corresponding to the almost straight mass–K luminosity relation at this age. Whether or not such a KLF would ever be seen in practice is debatable however, as stars this young would still be deeply embedded in their protostellar cocoons, making it unlikely that the "naked" PMS stars would be seen at this stage. By 0.3 Myr, features become apparent in the KLF, and by 0.7 Myr, there is a sharp peak in the KLF which can be traced to a sharp inflection at the corresponding point in the mass–K luminosity relation. This point of inflection is seen to move towards lower masses with time, and by 2 Myr the peak in the KLF has moved down close to our chosen mass cutoff at 0.08 $M_\odot$. By 10 Myr (not shown), the peak is long gone.

The inflection in the mass–K luminosity relation is a feature caused by

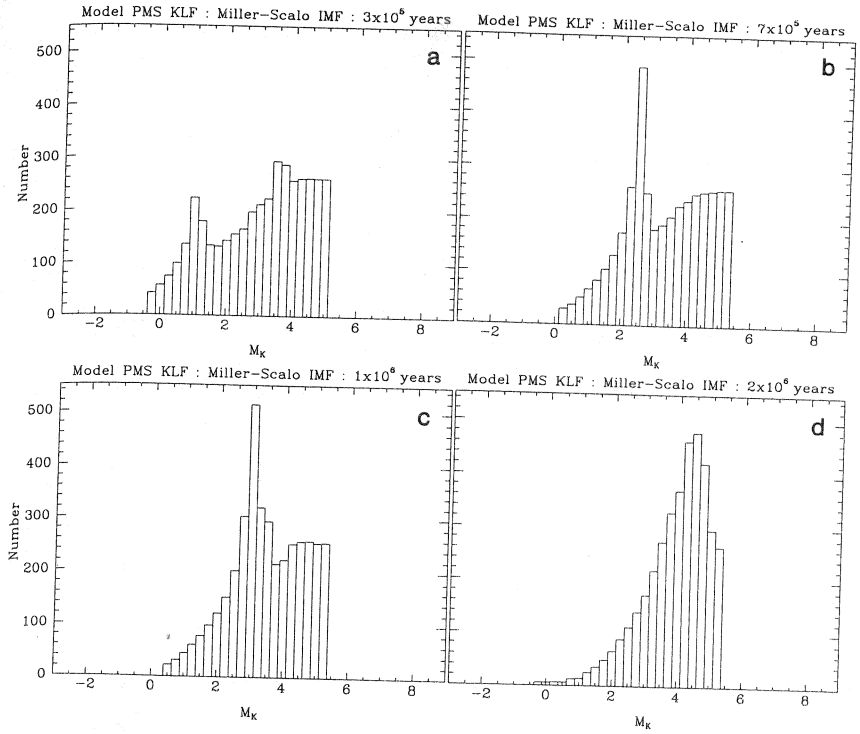

Figure 2 a,b,c,d. Model 2.2 μm (M_K) luminosity functions for a coeval cluster of low-mass stars at the same four ages shown in Fig. 1. The luminosity functions were calculated by convolving the mass–M_K relations with a Miller-Scalo IMF. Note the strong peak due to deuterium burning in the last three luminosity functions.

deuterium burning in contracting PMS stars. D-burning occurs when the Kelvin-Helmholtz contraction has proceeded far enough to raise the central temperature to $\sim 10^6$ K. For a 0.3 $M_\odot$ PMS star, D-burning occurs at an age of $\sim$1 Myr and lasts for $\sim$1 Myr, until most of the central deuterium is consumed. These time scales are fairly independent of the precise value of the initial deuterium abundance, although for reference, the Mazzitelli models were calculated using a deuterium abundance of 2×10^{-5} by mass, as derived for the solar neighborhood (York and Rogerson 1976). While deuterium is burning, the corresponding nuclear energy generation provides substantial support against continuing PMS contraction, i.e., for a while the star's radius and luminosity remain almost constant (see Fig. 2 of Mazzitelli and Moretti 1980). While the deuterium is burning strongly in stars of a given mass, D-burning is ending in slightly higher-mass stars, and has yet to begin in lower-mass stars. Thus, at the mass where peak D-burning is occurring (i.e., the mass whose time scale for the onset of strong D-burning is equal to the